Global fits of simplified models for dark matter with GAMBIT

II. Vector dark matter with an *s*-channel vector mediator

Christopher Chang[1,a]**, Pat Scott**[2]**, Tomás E. Gonzalo**[3]**, Felix Kahlhoefer**[3]**, Martin White**[4]

[1] School of Mathematics and Physics, The University of Queensland, St. Lucia, Brisbane, QLD 4072, Australia
[2] Quantum Brilliance Pty Ltd, The Australian National University, Daley Road, Acton ACT 2601, Australia
[3] Institute for Theoretical Particle Physics (TTP), Karlsruhe Institute of Technology (KIT), 76128 Karlsruhe, Germany
[4] ARC Centre of Excellence for Dark Matter Particle Physics & CSSM, Department of Physics, University of Adelaide, Adelaide, SA 5005

Abstract Global fits explore different parameter regions of a given model and apply constraints obtained at many energy scales. This makes it challenging to perform global fits of simplified models, which may not be valid at high energies. In this study, we derive a unitarity bound for a simplified vector dark matter model with an *s*-channel vector mediator, and apply it to global fits of this model with GAMBIT in order to correctly interpret missing energy searches at the LHC. Two parameter space regions emerge as consistent with all experimental constraints, corresponding to different annihilation modes of the dark matter. We show that although these models are subject to strong validity constraints, they are currently most strongly constrained by measurements less sensitive to the high-energy behaviour of the theory. Understanding when these models cannot be consistently studied will become increasingly relevant as they are applied to LHC Run 3 data.

Contents

[a]christopher.chang@uq.net.au

1 Introduction

As successful a theory as the Standard Model (SM) has been, there are many reasons for expecting it to exist within an even more descriptive particle theory. One of these reasons for beyond-Standard Model (BSM) physics is a number of astrophysical and cosmological observations that may require additional unseen matter [1–3]. The WIMP hypothesis postulates that this matter consists of a Weakly-Interacting Massive Particle, and is a popular theory as it may explain the observed cosmological relic abundance of dark matter (DM) [4] and be strongly constrained by near-future experiments [5].

WIMP candidates are present in many UV-complete theories including supersymmetric and extra-dimensional models. Rather than focus on these UV-complete theories, this study will instead focus on a simplified model. These are a class of effective theories where the particle that mediates interactions between DM and SM particles is explicitly included. In the limit of large mediator masses, the traditional DM effective theory is recovered. These models have been reviewed in detail in many works, including Refs. [5–12]. They have become the preferred method for modelling the simultaneous impact of low and high energy probes [13–15]. Studies of these models are often grouped to include multiple simplified models with different mediator and DM spins. This work will instead focus on a single model, in which a vector DM candidate interacts with a vector mediator in the *s*-channel. Details of this model are discussed in section 2. For global fits of models with scalar or fermion DM candidates, we refer the reader to the previous work in this series [16].

Models containing new vector particles can come with additional theoretical challenges in the high energy limit of the theory, arising from the requirement of

unitarity of the scattering matrix. Unitarity violation is a sign that the theory must be extended for it to be theoretically consistent; for example, unitarity violation in SM gauge boson interactions gave one of the early theoretical limits on the mass of the Higgs boson [17]. Likewise, unitarity arguments have been used to place an upper bound on the mass of DM particles that obtain their relic abundance through thermal freeze-out [18].

Vector DM simplified models have been studied in detail for both high and low energy experiments. For direct detection constraints, it has been shown that additional non-relativistic effective operators may arise in these models [19, 20], and that the use of polarized targets may distinguish between fermion and vector DM candidates [21]. Assuming a detection of signal events at the XENONnT experiment, prospects for finding these models during Run III of the Large Hadron Collider (LHC) in dijet searches [22] and mono-jet searches [23] have been studied along with relic density limits [24].

In this work, we derive a unitarity bound from the self-scattering of vector DM and show the similarity in constraint between this and the requirement of a physical decay width of the mediator. We follow this with a global fit of this model using GAMBIT v2.4, including the decay width and unitarity requirements in our calculations.

This paper is structured as follows. In Section 2, we describe the simplified model that we study, and the reasons behind the choice of couplings. In section 3, we derive a unitarity bound on this model. Section 4 describes the set of experimental constraints we use to perform a global fit of this model and section 5 provides our results. Finally, Section 6 briefly discusses the potential to observe these particles at near-future experiments and presents our conclusions. The samples from our scans, the corresponding GAMBIT plotting scripts and a detailed unitarity bound proof can be downloaded from Zenodo [25].

2 Model

The general form of the Lagrangian for a simplified model of vector DM X^μ coupled to quarks via a mediator V^μ with vector and axial-vector couplings is [23]

$$
\begin{aligned}
\mathcal{L}_{\text{BSM}} = & -\frac{1}{2} X^\dagger_{\mu\nu} X^{\mu\nu} + m^2_{\text{DM}} X^\dagger_\mu X^\mu - \frac{1}{4} F'_{\mu\nu} F'^{\mu\nu} \\
& - \frac{1}{2} m^2_{\text{M}} V_\mu V^\mu - h_3 V_\mu \bar{q} \gamma^\mu q - h_4 V_\mu \bar{q} \gamma^\mu \gamma^5 q \\
& - \frac{\lambda_{\text{DM}}}{2} (X^\dagger_\mu X^\mu)^2 - \frac{\lambda_{\text{M}}}{4} (V_\mu V^\mu)^2 \\
& - \frac{b_3}{2} V^2_\mu (X^\dagger_\nu X^\nu) - \frac{b_4}{2} (V^\mu V^\nu)(X^\dagger_\mu X_\nu) \\
& - [i b_5 X^\dagger_\nu \partial_\mu X^\nu V^\mu + b_6 X^\dagger_\mu \partial^\mu X_\nu V^\nu \\
& \quad + b_7 \epsilon_{\mu\nu\rho\sigma} (X^{\dagger\mu} \partial^\nu X^\rho) V^\sigma + \text{h.c.}],
\end{aligned}
$$
(1)

where $X_{\mu\nu}$ is the field strength tensor for the vector DM, and $F'_{\mu\nu}$ for the mediator.

To reduce the complexity of this simplified model and the dimensionality of the corresponding parameter space, we make a number of simplifying assumptions. First, we neglect any four-field interactions, which are expected to be irrelevant for phenomenology, and therefore set the couplings λ_{DM}, λ_{M}, b_3 and b_4 to zero. Furthermore, we assume that the simplified model conserves CP symmetry, which requires the real components of b_6 and b_7 in eq. (1) to vanish. Finally, to preserve the SM gauge structure, we concentrate on vector-like couplings of the mediator to SM quarks and set $h_4 = 0$.

With these restrictions, one finds that the imaginary components of b_6 and b_7 only give rise to interactions that vanish in the limit of zero momentum transfer, leading to strongly suppressed constraints from direct detection experiments. Including these couplings in our global fits would therefore lead to rather trivial results, while at the same time requiring significant additional work in order to correctly treat the non-relativistic effective operators $\mathcal{O}_{19}$ and $\mathcal{O}_{20}$ introduced in Ref. [20] and the interference between different operators in the simulation of LHC events. We therefore neglect these couplings in the present work and focus on the two interaction terms proportional to h_3 and b_5.

Therefore, the Lagrangian of the model we adopt is

$$
\begin{aligned}
\mathcal{L}_{\text{BSM}} = & -\frac{1}{2} X^\dagger_{\mu\nu} X^{\mu\nu} + m^2_{\text{DM}} X^\dagger_\mu X^\mu \\
& - \frac{1}{4} F'_{\mu\nu} F'^{\mu\nu} - \frac{1}{2} m^2_{\text{M}} V_\mu V^\mu + g_{\text{q}} V_\mu \bar{q} \gamma^\mu q \\
& - i g_{\text{DM}} \left(X^\dagger_\nu \partial_\mu X^\nu - (\partial_\mu X^{\dagger\nu}) X_\nu \right) V^\mu,
\end{aligned}
$$
(2)

where we choose to label the quark coupling as g_{q} and the DM coupling as g_{DM} to agree with our previous work [16]. Both couplings can be taken as purely real since any imaginary phase can be absorbed into a redefinition of the fields.

Perturbative unitarity breaks down in large regions of the parameter space of this model due to the poor high

energy behaviour of the longitudinal polarized modes of the vector DM. Following the same approach as Ref. [26], here we derive an approximate unitarity bound for this model in terms of the Mandelstam variable s, from scattering of vector DM

$$s \lesssim \frac{\sqrt{48\pi} m_{\mathrm{DM}}^2}{g_{\mathrm{DM}}} . \tag{3}$$

Section 3 derives this relation, and section 4.4 describes how unitarity was imposed on simulated collider events in our global scan. In Appendix A, we present the equivalent bound if the b_6 and b_7 couplings of eq. (1) are included alongside the b_5 coupling.

The onshell decay width of the mediator to a pair of DM particles, $V \to XX$, is

$$\Gamma_{\mathrm{DM}} = \frac{g_{\mathrm{DM}}^2 \sqrt{1 - \frac{4m_{\mathrm{DM}}^2}{m_{\mathrm{M}}^2}}}{192\pi m_{\mathrm{M}} m_{\mathrm{DM}}^4} \times \\ \left(m_{\mathrm{M}}^6 - 8m_{\mathrm{M}}^4 m_{\mathrm{DM}}^2 + 28m_{\mathrm{M}}^2 m_{\mathrm{DM}}^4 - 48m_{\mathrm{DM}}^6 \right), \tag{4}$$

and the width to a given pair i of SM quarks, $V \to q_i q_i$, is

$$\Gamma_{\mathrm{q}_i} = \frac{g_{\mathrm{q}}^2 \sqrt{1 - \frac{4m_{\mathrm{q}_i}^2}{m_{\mathrm{M}}^2}}}{4\pi m_{\mathrm{M}}} \left(m_{\mathrm{M}}^2 + 2m_{\mathrm{q}_i}^2 \right) . \tag{5}$$

The total width of the mediator should not exceed the mediator mass, or else the perturbative description of DM interactions via mediator exchange is expected to break down.

3 Unitarity Violation

3.1 Forming Unitarity constraints from partial waves

Unitarity bounds are formed from partial wave analysis of the scattering of vector DM particles. For examples on the use of this method, see e.g. Refs. [17, 26, 27]. From the requirement of partial wave unitarity, the scattering amplitude must obey the bounds

$$0 \leq \mathrm{Im}(\mathcal{M}_{ii}^J) \leq 1 , \tag{6}$$

and

$$|\mathrm{Re}(\mathcal{M}_{ii}^J)| \leq \frac{1}{2} . \tag{7}$$

Here $\mathcal{M}_{ii}^J$ is the full scattering matrix element between 2-particle states i where the initial and final state particles are the same (hence the repeated index i), for the Jth partial wave. Tree-level amplitudes are generally used

to form these bounds, assuming that the higher orders do not provide significant corrections to the amplitude. In this way, the resulting bound may be interpreted as a "perturbative unitarity" bound. In the case of zero initial and final total spin,

$$\mathcal{M}_{ii}^J(s) = \frac{1}{32\pi} \beta_{ii} \int_{-1}^{1} d\cos\theta P^J(\cos\theta) \mathcal{M}_{ii}(s, \cos\theta) . \tag{8}$$

Here $P^J(x)$ is the Legendre polynomial of order J, θ is the scattering angle and s is the square of the centre-of-mass energy. An additional factor of $1/\sqrt{2}$ must be applied to the right hand side for each initial or final state with identical particles. The term β_{ii} is a kinematic factor, which for a final state of equal mass DM particles becomes

$$\beta_{ii} = \frac{\sqrt{(s - (m_1 + m_2)^2)(s - (m_1 - m_2)^2)}}{s} \\ = \sqrt{\frac{s - 4m_{\mathrm{DM}}^2}{s}} . \tag{9}$$

In the high-energy limit ($s \to \infty$), β_{ii} approaches 1. As the zeroth order usually dominates, it is often sufficient to study

$$\mathcal{M}_{ii}^0(s) = \frac{\beta_{ii}}{64\pi} \int_{-1}^{1} d\cos\theta \mathcal{M}_{ii}(s, \cos\theta) . \tag{10}$$

In the following derivation, we consider the self-scattering of DM, rather than DM with its antiparticle. The particle-antiparticle scattering via s-channel mediator exchange will also face poor behaviour at high energies, however this will be effectively covered anyway by our additional requirement that the perturbative description of the off-shell decay width of the mediator (including to DM particle-antiparticle pairs) does not break down.

The tree level amplitude of DM self-scattering has contributions from t and u channel processes (see Figure 1), which can be derived separately, and summed together. This is most easily understood in the centre of mass frame, where for incoming particles (with momenta $p_{(1)}$ and $p_{(2)}$) and outgoing particles (with momenta $p_{(3)}$ and $p_{(4)}$),

$$\begin{aligned} p_{(1)} &= \left(\mathrm{E}, 0, 0, \mathrm{P}\right) \\ p_{(2)} &= \left(\mathrm{E}, 0, 0, -\mathrm{P}\right) \\ p_{(3)} &= \left(\mathrm{E}, \mathrm{P}\sin\theta, 0, \mathrm{P}\cos\theta\right) \\ p_{(4)} &= \left(\mathrm{E}, -\mathrm{P}\sin\theta, 0, -\mathrm{P}\cos\theta\right) . \end{aligned} \tag{11}$$

Here $\mathrm{E} = \frac{\mathrm{E_{cm}}}{2}$ is the incoming particle energy and P is the magnitude of the incoming momentum of each particle. The longitudinal polarisations will most strongly
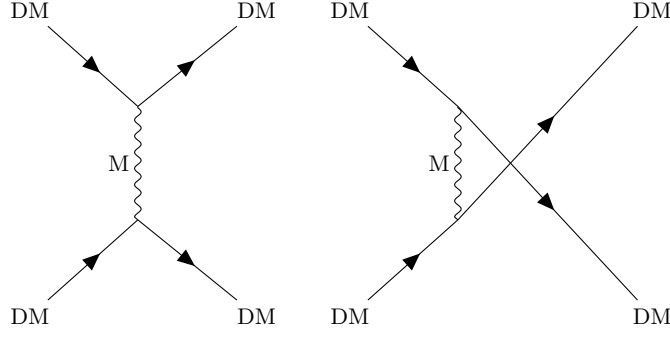
Fig. 1: t-channel (left) and u-channel (right) diagrams relevant for perturbative unitarity bounds.

violate unitarity, and so it is sufficient to solely form a bound from evaluating the amplitude for incoming longitudinally polarised DM particles. In the centre of mass frame, these are

$$
\begin{aligned}
\epsilon_{(1)} &= \frac{1}{m_{\mathrm{DM}}}\big(\mathrm{P}, 0, 0, \mathrm{E}\big) \\
\epsilon_{(2)} &= \frac{1}{m_{\mathrm{DM}}}\big(\mathrm{P}, 0, 0, -\mathrm{E}\big) \\
\epsilon_{(3)} &= \frac{1}{m_{\mathrm{DM}}}\big(\mathrm{P}, \mathrm{E}\sin\theta, 0, \mathrm{E}\cos\theta\big) \\
\epsilon_{(4)} &= \frac{1}{m_{\mathrm{DM}}}\big(\mathrm{P}, -\mathrm{E}\sin\theta, 0, -\mathrm{E}\cos\theta\big)\,.
\end{aligned}
\tag{12}
$$

The amplitude for t-channel DM-DM scattering at tree-level is

$$
\begin{aligned}
\mathcal{M} =\ & \frac{g_{\mathrm{DM}}^2}{k_{(t)}^2 - m_{\mathrm{M}}^2}\Big[\epsilon_{(3)\tau}(p_{(1)\mu} + p_{(3)\mu})\epsilon_{(1)}^\tau\Big] \\
& \times \left(g^{\mu\nu} - \frac{k_{(t)}^\mu k_{(t)}^\nu}{m_{\mathrm{M}}^2}\right)\Big[\epsilon_{(2)\sigma}(p_{(2)\nu} + p_{(4)\nu})\epsilon_{(4)}^\sigma\Big]\,,
\end{aligned}
\tag{13}
$$

where

$$
\begin{aligned}
k_{(t)} &= p_{(1)} - p_{(3)} = p_{(4)} - p_{(2)} \\
&= \big(0, -\mathrm{P}\sin\theta, 0, \mathrm{P}(1 - \cos\theta)\big)\,.
\end{aligned}
\tag{14}
$$

Evaluating this amplitude in the centre of mass frame gives

$$
\begin{aligned}
\mathcal{M}_t =\ & \frac{-g_{\mathrm{DM}}^2}{m_{\mathrm{DM}}^4\big(2\mathrm{P}^2(1 - \cos\theta) + m_{\mathrm{M}}^2\big)} \\
& \times \Big(\mathrm{P}^2 - (\mathrm{P}^2 + m_{\mathrm{DM}}^2)\cos\theta\Big)^2 \\
& \times \Big(6\mathrm{P}^2 + 4m_{\mathrm{DM}}^2 + 2\mathrm{P}^2\cos\theta\Big)\,.
\end{aligned}
\tag{15}
$$

Similarly, the scattering amplitude for u-channel DM DM scattering at tree-level is

$$
\begin{aligned}
\mathcal{M}_u =\ & \frac{-g_{\mathrm{DM}}^2}{m_{\mathrm{DM}}^4\big(2\mathrm{P}^2(1 + \cos\theta) + m_{\mathrm{M}}^2\big)} \\
& \times \Big(\mathrm{P}^2 + (\mathrm{P}^2 + m_{\mathrm{DM}}^2)\cos\theta\Big)^2 \\
& \times \Big(6\mathrm{P}^2 + 4m_{\mathrm{DM}}^2 - 2\mathrm{P}^2\cos\theta\Big)\,.
\end{aligned}
\tag{16}
$$

3.2 Unitarity Bound

The total amplitude of the scattering process is

$$
\mathcal{M}_{ii}(s, \cos\theta) = \mathcal{M}_t + \mathcal{M}_u\,.
\tag{17}
$$

Performing the integral in eq. (10) and substituting into eq. (7) gives the bound on parameters to satisfy unitarity

$$
\begin{aligned}
\Bigg| & \frac{g_{\mathrm{DM}}^2}{96\pi m_{\mathrm{DM}}^4(\frac{s}{2} - 2m_{\mathrm{DM}}^2)^3}\sqrt{\frac{s - 4m_{\mathrm{DM}}^2}{s}} \\
& \left(2\big((\tfrac{s}{2} - 2m_{\mathrm{DM}}^2)^2\big(\tfrac{s^2}{4}(m_{\mathrm{DM}}^2 - s)\right. \\
& + \frac{3m_{\mathrm{DM}}^2 s}{4}(3s - 4m_{\mathrm{DM}}^2) + 3m_{\mathrm{DM}}^4(\tfrac{s}{2} - 2m_{\mathrm{DM}}^2)\big) \\
& + \frac{3m_{\mathrm{M}}^2 s}{8}(s - 4m_{\mathrm{DM}}^2)(\tfrac{3s^2}{8} + \tfrac{1}{2}m_{\mathrm{DM}}^2 s - 4m_{\mathrm{DM}}^4 \\
& \left. + \frac{3m_{\mathrm{M}}^4 s^2}{32}(s - 4m_{\mathrm{DM}}^2)\big)\right. \\
& - 3\big(\frac{m_{\mathrm{M}}^2 s}{4} + m_{\mathrm{DM}}^2(\tfrac{s}{2} - 2m_{\mathrm{DM}}^2)\big)^2 \\
& \quad\quad \big(2s - 4m_{\mathrm{DM}}^2 + m_{\mathrm{M}}^2\big) \\
& \left.\ln\left(\frac{s - 4m_{\mathrm{DM}}^2 + m_{\mathrm{M}}^2}{m_{\mathrm{M}}^2}\right)\right)\Bigg| \leq \frac{1}{2}\,.
\end{aligned}
\tag{18}
$$

Since unitarity is increasingly violated as the collision energy increases, the limit $s \gg m_{\mathrm{DM}}^2$ is often taken in the literature. If this limit is taken, this bound simplifies to

$$
s \lesssim \frac{\sqrt{48\pi}\, m_{\mathrm{DM}}^2}{g_{\mathrm{DM}}}\,.
\tag{19}
$$

The validity of this limit breaks down for small DM masses and large couplings. In these cases, the complete bound eq. (18) should be used.

Even though the unitarity requirement above has been derived for the case of DM self-scattering, the resulting bound can be interpreted more generally as

the energy scale where the interactions between DM particles and the vector mediator become unphysical. We will therefore apply the unitarity bound from eq. (18) to any process in which a pair of DM particles is produced, with $\sqrt{s}$ being replaced by the invariant mass of the DM pair m_{inv}. In particular, this requirement will be implemented in our simulation of LHC monojet events (see section 4), where we will discard any event that violates the unitarity bound. In other words, we apply LHC constraints only on those regions of phase space where the simplified model predictions can be trusted, and set conservative bounds otherwise.

It is worth noting that for $m_{\text{DM}} < m_{\text{M}}/2$, we expect mono-jet production to proceed dominantly via an on-shell mediator, such that $m_{\text{inv}} \approx m_{\text{M}}$. Hence, for

$$m_{\text{M}}^2 \gtrsim \frac{\sqrt{48\pi} m_{\text{DM}}^2}{g_{\text{DM}}} , \qquad (20)$$

virtually all events will be removed by the unitarity requirement such that the LHC mono-jet bounds are effectively absent. However, parameter points in this region typically also violate the requirement on the decay width from eq. (21), such that they would be excluded from the analysis anyway.

3.3 Physical Decay Widths

Alongside unitarity violation, another indication that the model breaks down is that the decay width of the mediator becomes large, indicating the inapplicability of perturbation theory to the underlying scattering process. When the mediator is on-shell, this can be interpreted as a bound on the decay width

$$\Gamma(m_{\text{M}}) \leq m_{\text{M}} . \qquad (21)$$

We reject all points in parameter space that do not satisfy this bound. In the following we require that an analogous inequality also holds for the off-shell decay width when replacing m_{M} by $\sqrt{s}$:

$$\Gamma(\sqrt{s}) \leq \sqrt{s} . \qquad (22)$$

In the high energy limit, the bound on the off-shell decay width results in the requirement

$$s \leq \frac{\sqrt{192\pi} m_{\text{DM}}^2}{g_{\text{DM}}} . \qquad (23)$$

This differs from eq. (18) by a factor of 2 (the unitarity bound being the stricter of the two). When assuming high collision energies, it is therefore clear to see that the unitarity bound and off-shell decay width bound are practically interchangeable. Figure 2 shows a comparison between the unitarity constraint with and without
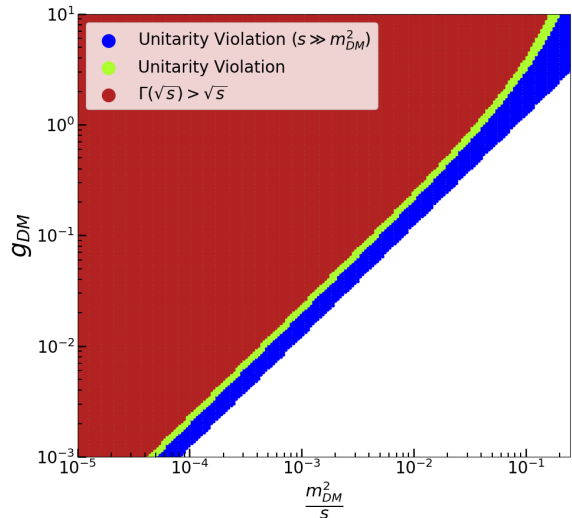

Fig. 2: Comparison between unitarity violation and unphysical decay widths for a demonstrative choice of parameters ($s = 10^8 \,\text{GeV}^2$, $m_{\text{M}} = \sqrt{s}$, $g_{\text{q}} = 0$, and varying m_{DM} and g_{DM}). The requirement of a physical off-shell decay width (green) excludes a smaller region than the requirement of unitarity (red), but follows a similar trend. Taking the high-energy limit of the unitarity bound is a consistently stricter cut on the parameter space (blue).

taking the high-energy limit, for a representative choice of parameters, along with the exclusion from requiring that the off-shell decay width is physical. The similarity between the unitarity and decay width conditions would suggest that for the choice of parameters shown, very little difference would be observed if the two were interchanged.

4 Constraints

Interactions between DM and SM quarks are constrained by many different measurements of astrophysical, cosmological and particle physics processes.

We use likelihoods, implemented in GAMBIT 2.3, for DM direct and indirect detection experiments, collider searches at the ATLAS and CMS experiments, and the measurement of the DM relic abundance. We generate the necessary model-specific GAMBIT module functions (including those used to store spectrum and decay information [28]) using the GAMBIT Universal Model Machine (GUM) [29]. This includes interfaces to backend codes that contain physics calculations for each DM observable. We apply the perturbative unitarity and physical off-shell decay width constraints described in section 3.2 to the calculation of collider signals, to ensure that calculations are accurate and the resulting

Experiment	$\ln \mathcal{L}^{\mathbf{bg}}$	$\ln \mathcal{L}^{\mathbf{max}}$
CDMSlite [30]	-16.68	
CRESST-II [31]	-27.59	
CRESST-III [32]	-27.22	
DarkSide 50 [33]	-0.09	
LUX 2016 [34]	-1.47	
PICO-60 [35, 36]	-1.496	
PandaX [37–39]	-6.121	
XENON1T [40]	-3.651	
LZ 2022 [41]	-4.636	
LHC Dijets [42–50]	0	
ATLAS monojet [51]	0	
CMS monojet [52]	0	
Fermi-LAT [53]	-33.245	
Planck 2018: Ωh^2 [54]		5.989
Nuisances (see Table 2)		-5.995

Table 1: All likelihoods included in our fits. We give the SM-only (i.e. background-only) log-likelihood $\ln \mathcal{L}^{\mathrm{bg}}$ for those that search for events above an SM background. For the rest, we give the highest achievable value of the log-likelihood $\ln \mathcal{L}^{\mathrm{max}}$, where the predicted value of the chosen observable or a nuisance parameter is exactly equal to its measured value.

limits are conservative; this is detailed in section 4.4. We reject parameter points that fail the requirement of a physical on-shell decay width of the mediator, before calculating their likelihood contributions.

Table 1 provides a summary of each likelihood that we include that is sensitive to BSM physics. For each likelihood, we provide either: $\ln \mathcal{L}^{\mathrm{bg}}$, the value that the likelihood takes purely from the SM, or $\ln \mathcal{L}^{\mathrm{max}}$, the best-case likelihood that can be achieved when parameters exactly match their centrally measured values.

For a detailed description of the implementation of each likelihood in GAMBIT, we refer the reader to the previous work in this series [16]. We provide brief summaries of each likelihood in the following subsections.

4.1 Relic Density

We use GUM to generate the CalcHEP v3.6.27 [55, 56] model files that are supplied to micrOMEGAs v3.6.9.2[57]. The relic density of DM is obtained with the DarkBit interface which uses micrOMEGAs to solve the Boltzmann equation for the number density of DM particles in thermal equilibrium, assuming a standard cosmological history. To form a likelihood from the relic abundance, we compare the calculated density to the *Planck* 2018 measurement of $\Omega_{\mathrm{DM,obs}} h^2 = 0.120 \pm 0.001$ [54] with a 1% theoretical error added in quadrature with the quoted *Planck* uncertainty.

We study both cases where the DM candidate is a subcomponent of the observed relic abundance and

where it fully saturates the abundance. When requiring that it saturates the relic abundance, we use the Planck measurement to define a Gaussian likelihood based on the predicted WIMP abundance. When allowing it to form a subcomponent, we modify this likelihood to be flat for predicted densities below the measurement; details can be found in Ref. [58].

4.2 Direct Detection

The parameters of a simplified DM model can be translated to the coefficients of the relevant operators in a non-relativistic EFT for WIMP-nucleon scattering, $c_i^{\mathrm{N}}(q^2)$. The single relevant operator and its coefficient for the vector DM simplified model in this study is [23].

$$c_1^{\mathrm{N}} = -\frac{2g_{\mathrm{q}} g_{\mathrm{DM}}^{\mathrm{V}}}{m_{\mathrm{M}}^2} \,, \tag{24}$$

which was supplied to DDCalc v2.2.0 [59, 60], to compute the differential cross-section and target element of interest.

We calculate direct detection likelihoods from the most recent XENON1T analysis [40], LUX 2016 [34], PandaX 2016, 2017 and 4T [37–39], CDMSlite [30], CRESST-II and CRESST-III [31, 32], PICO-60 2017 and 2019 [35, 36], DarkSide-50 [33] and LZ [41][1].

4.3 Indirect Detection

The model we study has two primary DM annihilation channels, annihilation to mediators and to quarks. Annihilation to a pair of mediators occurs as an *s*-wave process, and will be the primary annihilation channel when kinematically allowed ($m_{\mathrm{DM}} > m_{\mathrm{M}}$). When this channel is closed, the annihilation will occur to a pair of quarks, through the suppressed *p*-wave channel. We do not include *p*-wave contributions to the gamma-ray flux as they should not be large enough to impact searches toward dwarf spheroidals for the model we consider.

We compute the annihilation cross-section with CalcHEP, using the GUM interface to generate the required CalcHEP model files. We use the combined analysis of 15 dwarf spheroidal galaxies, Pass-8, performed by the *Fermi*-LAT Collaboration over 6 years of data taking [53], using gamLike v1.0.1 to compute the likelihood through its interface to DarkBit. DM annihilations at the centre of our galaxy are an alternative to dwarf spheroidal measurements. Since *Fermi*-LAT Galactic Centre limits are not as robust as limits from dwarf

---

[1]The description of how LZ is implemented is provided in Ref. [16].

spheroidals, we do not include them in this study. We do however briefly comment on the future impact of CTA observations on the parameter space of this model in section 6.

4.4 Monojet searches at the LHC

One of the primary channels via which to search for the model at colliders is the creation of a pair of final state WIMPs in association with a jet created by initial state radiation. This gives a signature of a single jet plus missing transverse energy ($\not{E}_\mathrm{T}$). We include the most current monojet searches from CMS and ATLAS searches with $137\,\mathrm{fb}^{-1}$ [52] and $139\,\mathrm{fb}^{-1}$ [51] of Run II integrated luminosity respectively.

To calculate the total production cross-section σ and the product of the efficiency and acceptance for passing the analysis kinematic selections ϵA, we perform simulation of Monte Carlo events with MadGraph_aMC@NLO [61] (v3.1.1), interfaced to Pythia v8.3 [62] for parton showering and hadronization. To form the quantity ϵA we pass these events through MadAnalysis 5 [63] and implement the ATLAS and CMS monojet analyses. Rather than perform this calculation for each parameter sample, we precompute a grid of cross sections (σ) and ϵA factors in advance, and interpolate them at runtime using ColliderBit [64].

An additional analysis cut is added to our implementations of the ATLAS and CMS kinematic selections, to remove any events which would violate the unitarity bound presented in section 3, replacing $\sqrt{s}$ with the invariant mass of the DM pair. When this cut becomes strong enough, there is a significant drop in the predicted acceptance of the analysis, and we can no longer make any sensible predictions regarding collider constraints. If no simulated events pass the unitarity cut, we expect the parameter point to be unobservable at the LHC and simply assign the background-only likelihood.

The interpolation grid we use is as follows:

- **mediator mass**: 17 values, $50\,\mathrm{GeV}$–$10\,\mathrm{TeV}$
- **DM/mediator mass ratio**: 16 values, 0.01–50
- **quark-mediator coupling**: 5 values, 0.01–1.0
- **DM-mediator coupling**: 7 values, 0.01–3.0

The grids for the mediator mass and couplings were chosen to be approximately equally spaced in log-space. The ratio of DM and mediator masses is more effective than the DM mass as a grid variable as it allows us to choose a grid with a higher density of points across the resonance region, where we expect rapid changes in predictions. Below the DM mass/mediator mass ratio of 0.01, we assume that we can safely extrapolate to small DM masses as the predicted signal should not

Parameters	Range
DM mass, m_DM	$[50, 10000]\,\mathrm{GeV}$
Mediator mass, m_M	$[50, 10000]\,\mathrm{GeV}$
quark-mediator coupling, g_q	$[0.01, 1.0]$
mediator-DM coupling (vector), g_DM^V	$[0.01, 3.0]$
Nuisance Parameters	**Value** ($\pm 3\sigma$ range)
Local DM density, ρ_0	$[0.2, 0.8]\,\mathrm{GeV\,cm}^{-3}$
Most probable DM speed, v_peak	$240(24)\,\mathrm{km\,s}^{-1}$
Galactic escape speed, v_esc	$528(75)\,\mathrm{km\,s}^{-1}$

Table 2: List of model and nuisance parameters and their corresponding scan ranges.

vary significantly. After removing any points with DM masses above the limits of our scan, this gives a total number of 6370 grid points.

4.5 Searches for dijet resonances

The presence of a mediating particle in the model may generate dijet events at colliders, with an invariant mass of approximately the mediator mass. Dijet resonance searches provide robust constraints on DM simplified models, where the extremely high multijet background must be removed with clever kinematic analysis cuts.

The cross-section for the production of a dijet resonance can be approximated as the product of the cross-section of mediator production and the branching ratio of the mediator into quarks, assuming that the narrow width approximation holds. When the ratio of the mediator decay width to mass is high, this approximation breaks down, and our treatment of dijet searches would become dubious. We briefly investigate the dependence of the model exclusion on this assumption in section 5.

We implement dijet limits provided by ATLAS and CMS [42–50] by scaling of the published limits of the mediator-quark coupling by the branching ratio into quarks, following the same approach as Refs. [16, 65]. These published limits are interpolated in m_M for each parameter point, and the likelihood is formed from the most constraining search for a given mediator mass. The combined coupling upper limits are provided in Figure 1 of Ref. [16].

4.6 Nuisance Parameter Likelihoods

Along with the model parameters in the model we study, we also include a set of nuisance parameters which are used in each of our astrophysical likelihoods. A complete list of these parameters is given in Table 2.

Relic Density	Best Fit m_{DM} (GeV)	Best Fit m_M (GeV)	Best Fit g_q	Best Fit g_{DM}^V	$\Delta \ln \mathcal{L}$
Upper limit	4950	9960	0.010	1.041	0.00
All DM	4570	9210	0.016	0.763	-0.45

Table 3: Approximate best-fit points for each scan. $\Delta \ln \mathcal{L}$ values are defined as $\ln \mathcal{L} - \ln \mathcal{L}^{\text{ideal}}$, where the ideal likelihood is the combination of background-only and maximum possible likelihoods detailed in Table 1.
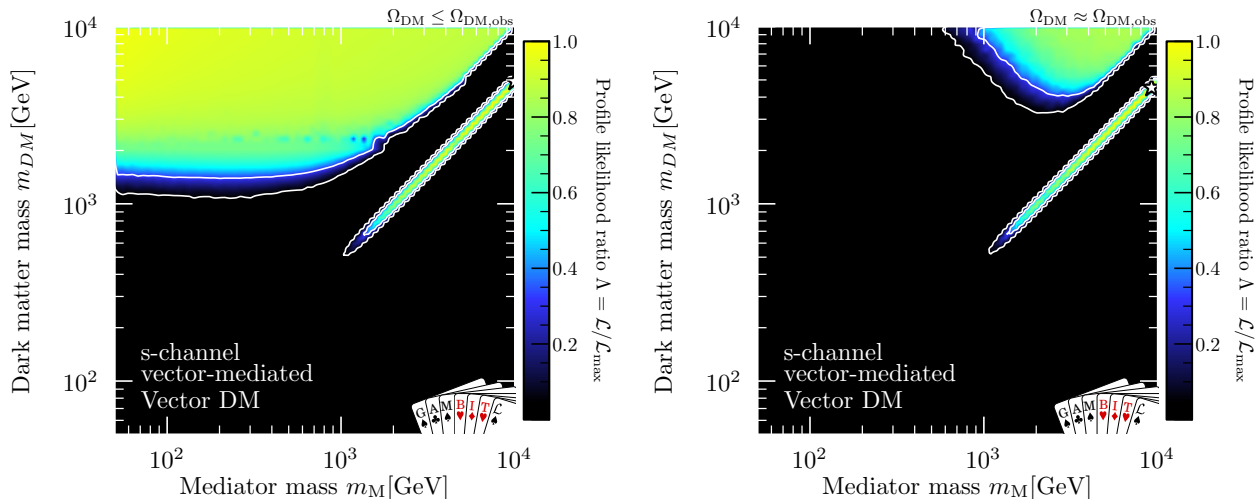
Fig. 3: Profile likelihood, profiled over couplings. The measured DM relic abundance is taken as an upper limit (left) or to be composed entirely of the vector DM candidate (right). 1σ and 2σ contours are shown in white, with the star representing the best-fit point.

We treat the local DM density ρ_0 following the standard procedure in DarkBit, where ρ_0 is assumed to be log-normally distributed, centred around $\rho_0 = 0.40\,\text{GeV}\,\text{cm}^{-3}$ and with an error $\sigma_{\rho_0} = 0.15\,\text{GeV}\,\text{cm}^{-3}$. The scan range of ρ_0 is asymmetric to reflect this distribution. 3σ ranges for all other nuisance parameters are provided in Table 2.

We treat the Milky Way halo in the same way as in several of our previous DM studies [16, 60, 66], where the DM velocity is assumed to follow a Maxwell-Boltzmann distribution. The peak velocity and Galactic escape velocity uncertainties are described by Gaussian likelihoods with $v_{\text{peak}} = 240 \pm 8\,\text{km}\,\text{s}^{-1}$ [67] and $v_{\text{esc}} = 528 \pm 25\,\text{km}\,\text{s}^{-1}$ (based on *Gaia* data [68]), respectively.

5 Results

We have performed a comprehensive scan of the model parameter space using the differential evolution sampler Diver v1.0.4 [69] with a convergence threshold of 10^{-6} and a population of 20 000, with an additional scan for DM masses below 2 TeV to improve sampling. We carried out two separate scans for the case where the observed DM relic density is taken as an upper limit or as a two-

sided measurement. Unlike the previous study in this series [16], scans with a capped LHC likelihood were not performed, as any small preferences over the background-only hypothesis in mono-jet searches were not found to occur within the surviving parameter space of the scan. A scan with a capped LHC likelihood would therefore produce results that were indistinguishable from its uncapped equivalent. Table 2 provides the full list of parameters and scan ranges. We adopt the same choice of scan ranges and sampling distributions of the masses and couplings as those in Ref. [16]. The parameter points that give the best likelihoods are given in Table 3.

The profile likelihood from combined constraints on the complex vector DM model is shown in Figures 3 and 4. The model prefers parameter regions where DM annihilation is efficient, and there are two regions corresponding to the two DM annihilation channels. Around the diagonal $m_M \approx 2m_{DM}$, the annihilation occurs close to a resonance into a pair of quarks. For regions where $m_{DM} > m_M$, the annihilation occurs as a t-channel process into a pair of mediator particles. Below approximately 500 GeV, the annihilation may not be great enough to prevent exclusion from direct detection constraints without leaving the limits of the scanned parameter ranges.
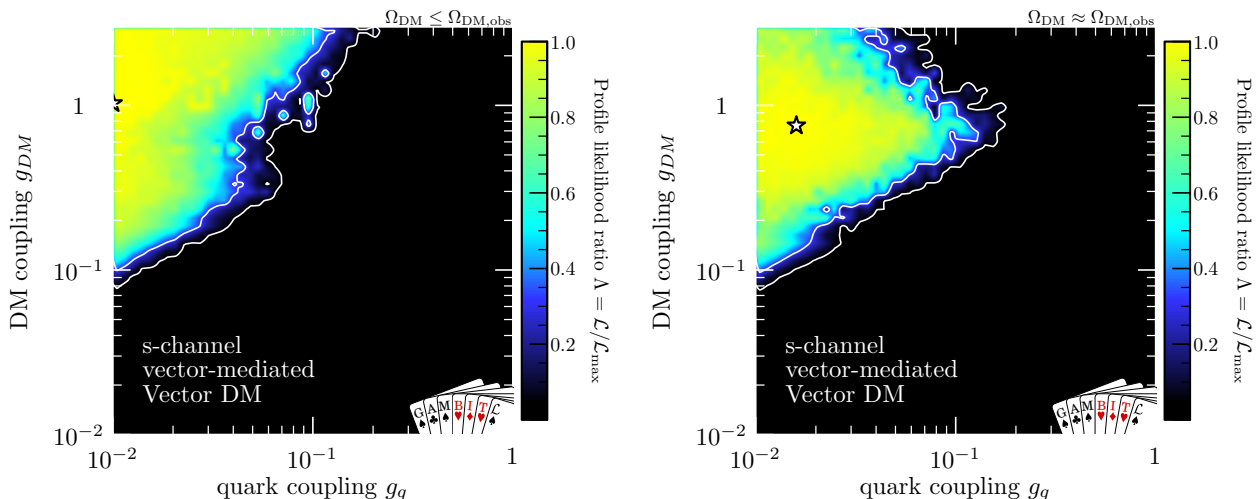
Fig. 4: Profile likelihood, profiling over mediator and DM masses, for a relic abundance upper limit (top) and a saturated relic abundance (bottom). 1σ and 2σ contours are shown in white, with the star representing the best-fit point.
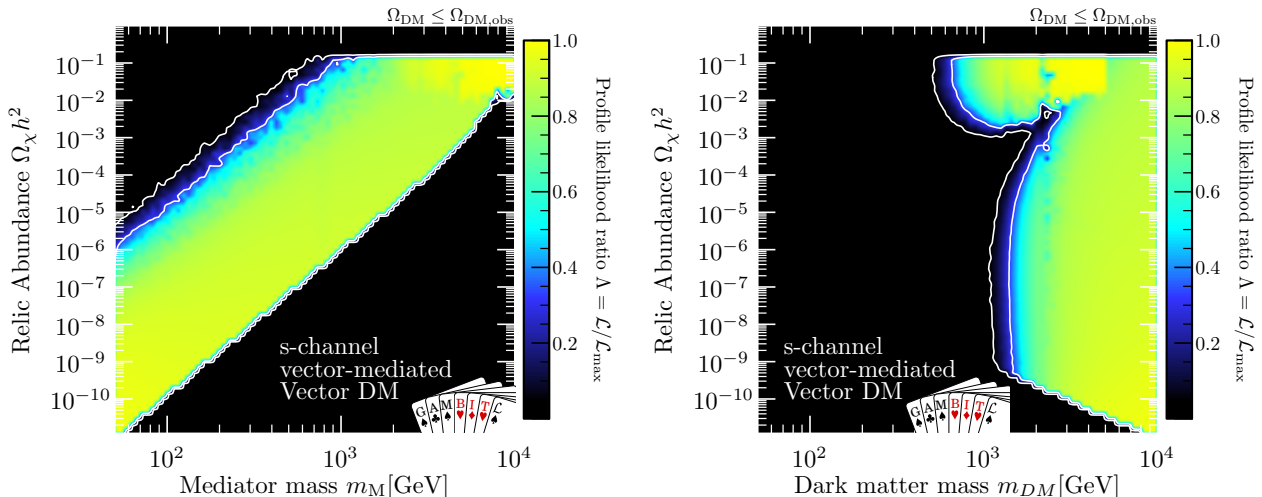

Fig. 5: DM relic abundance for the surviving parameter space, when taking the relic abundance measurement as an upper limit. We show the abundance both against mediator mass (left) and against DM mass (right). 1σ and 2σ contours are shown in white.

This shape is highly similar to those presented for a scalar DM candidate in Ref. [16]. This is because the strongest limits come from the direct detection experiments, which are dependent on the effective operators that are relevant, and this model shares the same relevant operator as the scalar DM model. The model survives for a greater proportion of the parameter space than the scalar DM model, despite the additional inclusion of PandaX-4T direct detection data in this work. The small variation in the profile likelihood around 2 TeV is a sampling artifact, and does not reflect any physical change in predictions.

Requiring that the DM relic abundance is saturated shrinks the surviving region to mediator masses above 1 TeV for the off-resonance region. For lower mediator masses, the non-relativistic effective coupling to nucleons is stronger and therefore expected signal at direct detection experiments is greater. Figure 5 (left) shows that at low mediator masses, the likelihood is higher in parameter regions where the model strongly underproduces DM to avoid tension with these experiments. As the strength of the direct detection constraints increases toward lower DM mass, the surviving parameter region also has a lower bound on the DM mass that may be seen in Figure 5 (right). The surviving region along the resonance does not depend strongly on whether the abundance likelihood is taken as a one-sided upper limit or a two-sided measurement. Measurements of dwarf spheroidal galaxies do not appear to have any strong influence on the profile likelihoods.
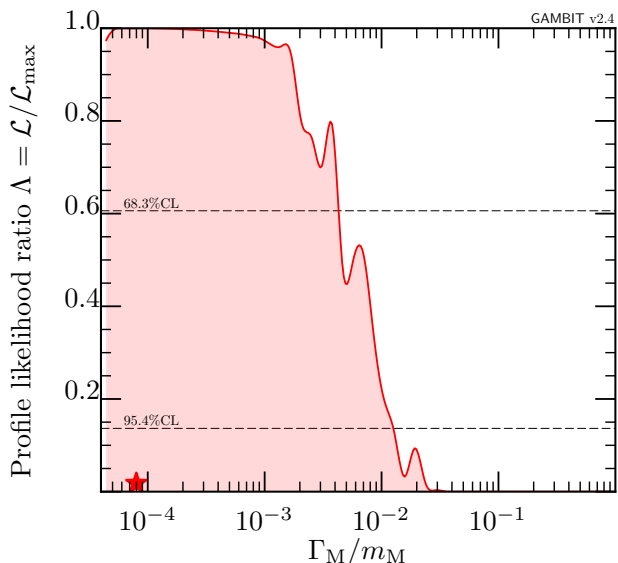
Fig. 6: Profile likelihood, as a function of the mediator width to mass ratio, profiled over all model parameters. 1σ and 2σ confidence limits are shown in black, with the red star representing the best-fit point.

We find that, in the surviving parameter regions, the decay width of the mediator is dominated by the partial width to quarks. Limits from dijet searches prevent mediator-quark couplings g_q above roughly 0.1 for most of the parameter space. This preference toward lower g_q reduces the effect of high decay widths, as the partial width to quarks is proportional to g_q^2. Fig 6 shows that within 2σ of the best-fit point, the decay width of the mediator does not exceed $0.02 m_M$, safely satisfying the narrow width requirement.

The effect of monojet searches cannot be seen directly on the results of the profile likelihood. For any model parameters where monojet searches would have sensitivity, these are strongly excluded by relic abundance limits and direct detection searches. The combined global fit therefore does not appear to be strongly affected by unitarity considerations. This conclusion might however change when considering a more general parameter space including also the couplings b_6 and b_7.

The best fit for each scan lies along the resonance, at the upper limits of the masses, and toward the lower limits of the quark coupling. In these regions, the relic abundance, and the strength of the direct detection signals are minimised. When the DM candidate is allowed to be a subcomponent of the observed DM density, this best-fit point approximately matches the background likelihood as the signals at any given DM experiment are almost entirely negligible. We compute an approximate p-value of the best-fit likelihood conditioned on the 'ideal' scenario (sum of background-only and max entries

in Table 1) for 1–2 effective degrees of freedom. Further explanation of the construction of this particular p-value can be found in Ref. [70]. Neither case (saturated or subdominant DM) is disfavoured, returning p-values of 0.3 and above.

We limited the couplings to be no lower than 0.01, in order to target parameter regions where unitarity violation was most likely to cause issues without introducing large hierarchies between couplings. If the scan range was expanded to include smaller g_q, it can be seen from Figure 4 how the size of the surviving parameter space should increase. Expanding the lower limit on g_{DM} will only expand the surviving space if g_q is also expanded. For the parameters scanned over in this work, the model is excluded for lower g_{DM}, as there cannot be sufficient annihilation of the thermal DM abundance.

6 Discussion

In this work, we have derived a unitarity bound for a simplified model with a vector DM candidate that interacts with SM quarks via an s-channel vector mediator. We showed that this unitarity bound is highly similar to the bound on the model parameters one would require from the behaviour of the off-shell decay width, which is another challenge that plagues these theories. Applying this bound to simulated collider events, we performed a global scan of this model with GAMBIT. We found that in all of the simulated parameter regions where the unitarity of the model may come into question or the decay of the mediator becomes unphysical, the model is excluded by experiments that are less sensitive to the high energy behaviour of the theory. Since the model exclusion most strongly comes from direct detection experiments and relic abundance limits, the surviving parameter space is split in two by the DM annihilation channels. The overall result is a series of limits that are highly similar to, but slightly weaker than, those found for corresponding scalar and fermionic DM models in the previous study in this series [16].

In the coming years, many experiments are expected to take data that may be used to constrain the model that we consider. In Figure 7 we show the predicted number of signal counts at the next-generation liquid Xenon direct detection experiment, DARWIN [71]. Within the surviving parameter space of the model, up to several hundred recoil events may be observed. Depending on how effectively the background can be rejected, a large portion of the surviving parameter space in these scans may be ruled out in the absence of any signal measurements.

We also checked the extent to which future observations by the Cherenkov Telescope Array (CTA) would
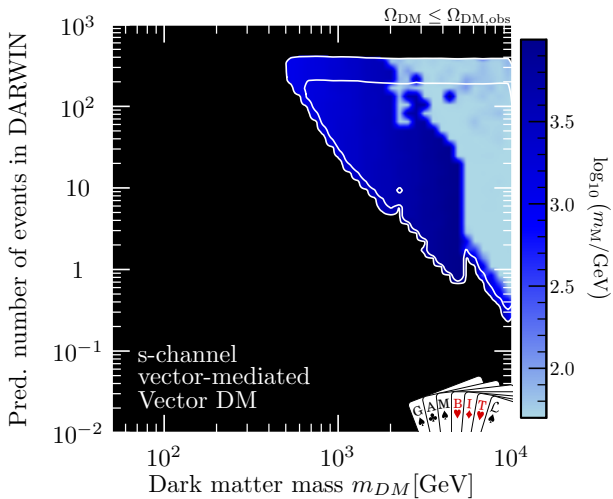
Fig. 7: Predicted number of signal events in the DARWIN experiment, coloured by the mediator mass. 1σ and 2σ profile likelihood contours are shown in white.

constrain the model, using the same methods as in Ref. [16]. None of the currently viable parameter space will be probed by CTA, with the parameter space along the resonance region far out of reach because the annihilations occur through the p-wave suppressed channel to quarks.

Finally, we note that further constraints can be expected from Run 3 of the LHC and the subsequent high-luminosity phase, as well as future colliders. In order to correctly interpret these constraints, it will become increasingly important to understand the high-energy behaviour of simplified models.

Acknowledgements

A: Unitarity Bound including b_6 and b_7 couplings

If the b_6 and b_7 couplings from eq. (1) are allowed to be nonzero, the unitarity bound becomes

$$
\frac{1}{32\pi m_{\mathrm{DM}}^4 (\frac{s}{2} - 2m_{\mathrm{DM}}^2)^3} \sqrt{\frac{s - 4m_{\mathrm{DM}}^2}{s}} \left| \frac{b_5^2}{3} \left[2\left((\frac{s}{2} - 2m_{\mathrm{DM}}^2)^2 (\frac{s^2}{4}(m_{\mathrm{DM}}^2 - s) + \frac{3m_{\mathrm{DM}}^2 s}{4}(3s - 4m_{\mathrm{DM}}^2) \right. \right. \right.
$$

$$
+ 3m_{\mathrm{DM}}^4 (\frac{s}{2} - 2m_{\mathrm{DM}}^2)) + \frac{3m_{\mathrm{M}}^2 s}{8}(s - 4m_{\mathrm{DM}}^2)(\frac{3s^2}{8} + \frac{1}{2}m_{\mathrm{DM}}^2 s - 4m_{\mathrm{DM}}^4) + \frac{3m_{\mathrm{M}}^4 s^2}{32}(s - 4m_{\mathrm{DM}}^2))
$$

$$
\left. - 3(\frac{m_{\mathrm{M}}^2 s}{4} + m_{\mathrm{DM}}^2 (\frac{s}{2} - 2m_{\mathrm{DM}}^2))^2 (2s - 4m_{\mathrm{DM}}^2 + m_{\mathrm{M}}^2) \ln\left(\frac{s - 4m_{\mathrm{DM}}^2 + m_{\mathrm{M}}^2}{m_{\mathrm{M}}^2}\right) \right]
$$

$$
+ \frac{b_5 \mathrm{Im}(b_6) s}{12} \left[-(2s - 8m_{\mathrm{DM}}^2)\left((\frac{s}{2} - 2m_{\mathrm{DM}}^2)^2 (-2s + 9m_{\mathrm{DM}}^2) - 3m_{\mathrm{M}}^2(\frac{s}{2} - 2m_{\mathrm{DM}}^2)(-\frac{3s}{4} - m_{\mathrm{DM}}^2) + \frac{3m_{\mathrm{M}}^4 s}{4} \right) \right.
$$

$$
\left. + 6m_{\mathrm{M}}^2(2s - 8m_{\mathrm{DM}}^2 + m_{\mathrm{M}}^2)(m_{\mathrm{DM}}^2(\frac{s}{2} - 2m_{\mathrm{DM}}^2) + \frac{m_{\mathrm{M}}^2 s}{4}) \ln\left(\frac{s - 4m_{\mathrm{DM}}^2 + m_{\mathrm{M}}^2}{m_{\mathrm{M}}^2}\right) \right]
$$

$$
- \frac{\mathrm{Re}(b_6)^2}{24} \left[s(2s - 8m_{\mathrm{DM}}^2)\left(s(\frac{s}{2} - 2m_{\mathrm{DM}}^2)^2 - 3\frac{m_{\mathrm{M}}^2 s}{4}(\frac{s}{2} - 2m_{\mathrm{DM}}^2) + \frac{3m_{\mathrm{M}}^4 s}{4} \right) + \frac{9m_{\mathrm{M}}^6 s^2}{2} \ln\left(\frac{s - 4m_{\mathrm{DM}}^2 + m_{\mathrm{M}}^2}{m_{\mathrm{M}}^2}\right) \right.
$$

$$
\left. + \frac{6s^2}{m_{\mathrm{M}}^2}(\frac{s}{2} - 2m_{\mathrm{DM}}^2)^4 - 4s^2(\frac{s}{2} - 2m_{\mathrm{DM}}^2)^3 + 12m_{\mathrm{M}}^2 s^2(\frac{s}{4} - m_{\mathrm{DM}}^2)^2 - 6m_{\mathrm{M}}^4 s^2(\frac{s}{4} - m_{\mathrm{DM}}^2) \right]
$$

$$
- \frac{\mathrm{Im}(b_6)^2 s}{24} \left[(2s - 8m_{\mathrm{DM}}^2)\left((\frac{s}{2} - 2m_{\mathrm{DM}}^2)^2 (2s - 6m_{\mathrm{DM}}^2) - 3m_{\mathrm{M}}^2(\frac{s}{2} - 2m_{\mathrm{DM}}^2)(\frac{3s}{4} - 2m_{\mathrm{DM}}^2) - \frac{3m_{\mathrm{M}}^4 s}{4} \right) \right.
$$

$$
\left. + 6m_{\mathrm{M}}^4\left((\frac{s}{2} - 2m_{\mathrm{DM}}^2)(s - 2m_{\mathrm{DM}}^2) + \frac{m_{\mathrm{M}}^2 s}{4} \right) \ln\left(\frac{s - 4m_{\mathrm{DM}}^2 + m_{\mathrm{M}}^2}{m_{\mathrm{M}}^2}\right) \right]
$$

$$
\left. - \mathrm{Re}(b_7)^2 m_{\mathrm{DM}}^4 s \left[2(\frac{s}{2} - 2m_{\mathrm{DM}}^2)(\frac{s}{2} - 2m_{\mathrm{DM}}^2 + m_{\mathrm{M}}^2) + m_{\mathrm{M}}^2\left(-s + 4m_{\mathrm{DM}}^2 - m_{\mathrm{M}}^2 \right) \ln\left(\frac{s - 4m_{\mathrm{DM}}^2 + m_{\mathrm{M}}^2}{m_{\mathrm{M}}^2}\right) \right] \right| \leq \frac{1}{2},
$$

(A.1)

where b_5 corresponds to the coupling g_{DM} in the model we adopt. For the proof of the relation, we refer the reader to the supplementary Zenodo record for this study [25]. The b_6 and b_7 couplings are split into their real and imaginary components, with the CP-violating couplings left in for completion. The imaginary component of the b_7 cancels in the formation of the bound. In the limit of high s, this simplifies to

$$
\left| -\frac{b_5^2 s^2}{96\pi m_{\mathrm{DM}}^4} + \frac{b_5 \mathrm{Im}(b_6) s^2}{48\pi m_{\mathrm{DM}}^4} - \frac{\mathrm{Re}(b_6)^2 s^3}{256\pi m_{\mathrm{M}}^2 m_{\mathrm{DM}}^4} - \frac{\mathrm{Im}(b_6)^2 s^2}{96\pi m_{\mathrm{DM}}^4} - \frac{\mathrm{Re}(b_7)^2}{8\pi} \right| \leq \frac{1}{2} .
$$

(A.2)

The term from the real component of the b_7 coupling is independent of s.

References

1. F. Zwicky, *Die Rotverschiebung von extragalaktischen Nebeln*, Helvetica Physica Acta **6** (1933) 110–127.

2. D. Clowe, M. Bradač, *et. al.*, *A Direct Empirical Proof of the Existence of Dark Matter*, ApJ **648** (2006) L109–L113, [astro-ph/0608407].

3. D. N. Spergel, R. Bean, *et. al.*, *Three-Year Wilkinson Microwave Anisotropy Probe (WMAP) Observations: Implications for Cosmology*, ApJS **170** (2007) 377–408, [astro-ph/0603449].

4. B. W. Lee and S. Weinberg, *Cosmological Lower Bound on Heavy Neutrino Masses*, Phys. Rev. Lett. **39** (1977) 165–168.

5. G. Arcadi, M. Dutra, *et. al.*, *The waning of the WIMP? A review of models, searches, and constraints*, Eur. Phys. J. **C78** (2018) 203, [arXiv:1703.07364].

6. J. Abdallah *et. al.*, *Simplified Models for Dark Matter Searches at the LHC*, Phys. Dark Univ. **9-10** (2015) 8–23, [arXiv:1506.03116].

7. C. Arina, *Impact of cosmological and astrophysical constraints on dark matter simplified models*, Front. Astron. Space Sci. **5** (2018) 30, [arXiv:1805.04290].

8. A. De Simone and T. Jacques, *Simplified models vs. effective field theory approaches in dark matter searches*, Eur. Phys. J. C **76** (2016) 367, [arXiv:1603.08002].

9. A. Albert *et. al.*, *Recommendations of the LHC Dark Matter Working Group: Comparing LHC searches for dark matter mediators in visible and invisible decay channels and calculations of the thermal relic density*, Phys. Dark Univ. **26** (2019) 100377, [arXiv:1703.05703].

10. A. Boveia *et. al.*, *Recommendations on presenting LHC searches for missing transverse energy signals using simplified s-channel models of dark matter*, Phys. Dark Univ. **27** (2020) 100365, [arXiv:1603.04156].

11. F. Kahlhoefer, *Review of LHC Dark Matter Searches*, Int. J. Mod. Phys. A **32** (2017) 1730006, [arXiv:1702.02430].

12. E. Morgante, *Simplified Dark Matter Models*, Adv. High Energy Phys. **2018** (2018) 5012043, [arXiv:1804.01245].

13. F. D'Eramo, B. J. Kavanagh, and P. Panci, *You can hide but you have to run: direct detection with vector mediators*, JHEP **08** (2016) 111, [arXiv:1605.04917].

14. L. M. Carpenter, R. Colburn, J. Goodman, and T. Linden, *Indirect Detection Constraints on s and t Channel Simplified Models of Dark Matter*, Phys. Rev. D **94** (2016) 055027, [arXiv:1606.04138].

15. D. Abercrombie *et. al.*, *Dark Matter Benchmark Models for Early LHC Run-2 Searches: Report of the ATLAS/CMS Dark Matter Forum*, Phys. Dark Univ. **26** (2019) 100371, [arXiv:1507.00966].

16. C. Chang, P. Scott, *et. al.*, *Global fits of simplified models for dark matter with GAMBIT I. Scalar and fermionic models with s-channel vector mediators*, [arXiv:2209.13266].

17. B. W. Lee, C. Quigg, and H. B. Thacker, *The Strength of Weak Interactions at Very High-Energies and the Higgs Boson Mass*, Phys. Rev. Lett. **38** (1977) 883–885.

18. K. Griest and M. Kamionkowski, *Unitarity Limits on the Mass and Radius of Dark Matter Particles*, Phys. Rev. Lett. **64** (1990) 615.

19. J. B. Dent, L. M. Krauss, J. L. Newstead, and S. Sabharwal, *General analysis of direct dark matter detection: From microphysics to observational signatures*, Phys. Rev. D **92** (2015) 063515, [arXiv:1505.03117].

20. R. Catena, K. Fridell, and M. B. Krauss, *Non-relativistic Effective Interactions of Spin 1 Dark Matter*, JHEP **08** (2019) 030, [arXiv:1907.02910].

21. R. Catena, K. Fridell, and V. Zema, *Direct detection of fermionic and vector dark matter with polarised targets*, JCAP **11** (2018) 018, [arXiv:1810.01515].

22. S. Baum, R. Catena, and M. B. Krauss, *Impact of a XENONnT signal on LHC dijet searches*, JHEP **07** (2019) 015, [arXiv:1812.01594].

23. S. Baum, R. Catena, J. Conrad, K. Freese, and M. B. Krauss, *Determining dark matter properties with a XENONnT/LZ signal and LHC Run 3 monojet searches*, Phys. Rev. D **97** (2018) 083002, [arXiv:1709.06051].

24. R. Catena, J. Conrad, and M. B. Krauss, *Compatibility of a dark matter discovery at XENONnT or LZ with the WIMP thermal production mechanism*, Phys. Rev. D **97** (2018) 103002, [arXiv:1712.07969].

25. GAMBIT Collaboration, *Supplementary Data: Global fits if simplified models for dark matter with GAMBIT II. Vector dark matter with an s-channel vector mediator.*, (2023), https://zenodo.org/record/7710586.

26. F. Kahlhoefer, K. Schmidt-Hoberg, T. Schwetz, and S. Vogl, *Implications of unitarity and gauge invariance for simplified dark matter models*, JHEP **02** (2016) 016, [arXiv:1510.02110].

27. M. S. Chanowitz, M. A. Furman, and I. Hinchliffe, *Weak Interactions of Ultraheavy Fermions. 2.*, *Nucl. Phys. B* **153** (1979) 402–430.

28. GAMBIT Models Workgroup: P. Athron, C. Balázs, *et. al.*, *SpecBit, DecayBit and PrecisionBit: GAMBIT modules for computing mass spectra, particle decay rates and precision observables*, *Eur. Phys. J. C* **78** (2018) 22, [arXiv:1705.07936].

29. GAMBIT Collaboration: S. Bloor, T. E. Gonzalo, *et. al.*, *The GAMBIT Universal Model Machine: from Lagrangians to likelihoods*, *Eur. Phys. J. C* **81** (2021) 1103, [arXiv:2107.00030].

30. SuperCDMS: R. Agnese *et. al.*, *New Results from the Search for Low-Mass Weakly Interacting Massive Particles with the CDMS Low Ionization Threshold Experiment*, *Phys. Rev. Lett.* **116** (2016) 071301, [arXiv:1509.02448].

31. CRESST: G. Angloher *et. al.*, *Results on light dark matter particles with a low-threshold CRESST-II detector*, *Eur. Phys. J.* **C76** (2016) 25, [arXiv:1509.01515].

32. CRESST: A. H. Abdelhameed *et. al.*, *First results from the CRESST-III low-mass dark matter program*, *Phys. Rev. D* **100** (2019) 102002, [arXiv:1904.00498].

33. DarkSide: P. Agnes *et. al.*, *DarkSide-50 532-day Dark Matter Search with Low-Radioactivity Argon*, *Phys. Rev. D* **98** (2018) 102006, [arXiv:1802.07198].

34. LUX: D. S. Akerib *et. al.*, *Results from a search for dark matter in the complete LUX exposure*, *Phys. Rev. Lett.* **118** (2017) 021303, [arXiv:1608.07648].

35. PICO: C. Amole *et. al.*, *Dark Matter Search Results from the PICO-60 C_3F_8 Bubble Chamber*, *Phys. Rev. Lett.* **118** (2017) 251301, [arXiv:1702.07666].

36. PICO: C. Amole *et. al.*, *Dark Matter Search Results from the Complete Exposure of the PICO-60 C_3F_8 Bubble Chamber*, *Phys. Rev. D* **100** (2019) 022001, [arXiv:1902.04031].

37. PandaX-II: A. Tan *et. al.*, *Dark Matter Results from First 98.7 Days of Data from the PandaX-II Experiment*, *Phys. Rev. Lett.* **117** (2016) 121303, [arXiv:1607.07400].

38. PandaX-II: X. Cui *et. al.*, *Dark Matter Results From 54-Ton-Day Exposure of PandaX-II Experiment*, *Phys. Rev. Lett.* **119** (2017) 181302, [arXiv:1708.06917].

39. PandaX-4T: Y. Meng *et. al.*, *Dark Matter Search Results from the PandaX-4T Commissioning Run*, *Phys. Rev. Lett.* **127** (2021) 261802, [arXiv:2107.13438].

40. XENON: E. Aprile *et. al.*, *Dark Matter Search Results from a One Ton-Year Exposure of XENON1T*, *Phys. Rev. Lett.* **121** (2018) 111302, [arXiv:1805.12562].

41. LZ: J. Aalbers *et. al.*, *First Dark Matter Search Results from the LUX-ZEPLIN (LZ) Experiment*, arXiv:2207.03764.

42. CMS: A. M. Sirunyan *et. al.*, *Search for high mass dijet resonances with a new background prediction method in proton-proton collisions at $\sqrt{s} = 13$ TeV*, *JHEP* **05** (2020) 033, [arXiv:1911.03947].

43. ATLAS: G. Aad *et. al.*, *Search for new resonances in mass distributions of jet pairs using 139 fb^{-1} of pp collisions at $\sqrt{s} = 13$ TeV with the ATLAS detector*, *JHEP* **03** (2020) 145, [arXiv:1910.08447].

44. ATLAS: M. Aaboud *et. al.*, *Search for low-mass dijet resonances using trigger-level jets with the ATLAS detector in pp collisions at $\sqrt{s} = 13$ TeV*, *Phys. Rev. Lett.* **121** (2018) 081801, [arXiv:1804.03496].

45. CDF: T. Aaltonen *et. al.*, *Search for new particles decaying into dijets in proton-antiproton collisions at $\sqrt{s} = 1.96$ TeV*, *Phys. Rev. D* **79** (2009) 112002, [arXiv:0812.4036].

46. ATLAS: M. Aaboud *et. al.*, *Search for light resonances decaying to boosted quark pairs and produced in association with a photon or a jet in proton-proton collisions at $\sqrt{s} = 13$ TeV with the ATLAS detector*, *Phys. Lett. B* **788** (2019) 316–335, [arXiv:1801.08769].

47. ATLAS Collaboration, *Search for boosted resonances decaying to two b-quarks and produced in association with a jet at $\sqrt{s} = 13$ TeV with the ATLAS detector*, 2018.

48. CMS: A. M. Sirunyan *et. al.*, *Search for low mass vector resonances decaying into quark-antiquark pairs in proton-proton collisions at $\sqrt{s} = 13$ TeV*, *Phys. Rev. D* **100** (2019) 112007, [arXiv:1909.04114].

49. ATLAS: M. Aaboud *et. al.*, *Search for low-mass resonances decaying into two jets and produced in association with a photon using pp collisions at $\sqrt{s} = 13$ TeV with the ATLAS detector*, *Phys. Lett. B* **795** (2019) 56–75, [arXiv:1901.10917].

50. CMS: A. M. Sirunyan *et. al.*, *Search for Low-Mass Quark-Antiquark Resonances Produced in Association with a Photon at $\sqrt{s} = 13$ TeV*, *Phys. Rev. Lett.* **123** (2019) 231803, [arXiv:1905.10331].

51. ATLAS: G. Aad *et. al.*, *Search for new phenomena in events with an energetic jet and missing*

transverse momentum in pp collisions at $\sqrt{s} = 13$ TeV with the ATLAS detector, arXiv:2102.10874.

52. CMS collaboration, *Search for new particles in events with energetic jets and large missing transverse momentum in proton-proton collisions at $\sqrt{s} = 13$ TeV*, *CMS-PAS-EXO-20-004* (2021).

53. Fermi-LAT: M. Ackermann *et. al.*, *Searching for Dark Matter Annihilation from Milky Way Dwarf Spheroidal Galaxies with Six Years of Fermi Large Area Telescope Data*, *Phys. Rev. Lett.* **115** (2015) 231301, [arXiv:1503.02641].

54. Planck: N. Aghanim *et. al.*, *Planck 2018 results. VI. Cosmological parameters*, *Astron. Astrophys.* **641** (2020) A6, [arXiv:1807.06209].

55. A. Pukhov, *CalcHEP 2.3: MSSM, structure functions, event generation, batchs, and generation of matrix elements for other packages*, hep-ph/0412191.

56. A. Belyaev, N. D. Christensen, and A. Pukhov, *CalcHEP 3.4 for collider physics within and beyond the Standard Model*, *Comp. Phys. Comm.* **184** (2013) 1729–1769, [arXiv:1207.6082].

57. G. Bélanger, F. Boudjema, A. Pukhov, and A. Semenov, *micrOMEGAs4.1: Two dark matter candidates*, *Comp. Phys. Comm.* **192** (2015) 322–329, [arXiv:1407.6129].

58. GAMBIT Collaboration: P. Athron, C. Balázs, *et. al.*, *GAMBIT: The Global and Modular Beyond-the-Standard-Model Inference Tool*, *Eur. Phys. J. C* **77** (2017) 784, [arXiv:1705.07908]. Addendum in [73].

59. GAMBIT Dark Matter Workgroup: T. Bringmann, J. Conrad, *et. al.*, *DarkBit: A GAMBIT module for computing dark matter observables and likelihoods*, *Eur. Phys. J. C* **77** (2017) 831, [arXiv:1705.07920].

60. GAMBIT Collaboration: P. Athron *et. al.*, *Global analyses of Higgs portal singlet dark matter models using GAMBIT*, *Eur. Phys. J. C* **79** (2019) 38, [arXiv:1808.10465].

61. J. Alwall, M. Herquet, F. Maltoni, O. Mattelaer, and T. Stelzer, *MadGraph 5 : Going Beyond*, *JHEP* **06** (2011) 128, [arXiv:1106.0522].

62. T. Sjostrand, S. Mrenna, and P. Z. Skands, *A Brief Introduction to PYTHIA 8.1*, *Comput. Phys. Commun.* **178** (2008) 852–867, [arXiv:0710.3820].

63. E. Conte, B. Fuks, and G. Serret, *MadAnalysis 5, A User-Friendly Framework for Collider Phenomenology*, *Comput. Phys. Commun.* **184** (2013) 222–256, [arXiv:1206.1599].

64. GAMBIT Collider Workgroup: C. Balázs, A. Buckley, *et. al.*, *ColliderBit: a GAMBIT module for the calculation of high-energy collider observables and likelihoods*, *Eur. Phys. J. C* **77** (2017) 795, [arXiv:1705.07919].

65. E. Bagnaschi *et. al.*, *Global Analysis of Dark Matter Simplified Models with Leptophobic Spin-One Mediators using MasterCode*, *Eur. Phys. J. C* **79** (2019) 895, [arXiv:1905.00892].

66. GAMBIT: P. Athron *et. al.*, *Thermal WIMPs and the scale of new physics: global fits of Dirac dark matter effective field theories*, *Eur. Phys. J. C* **81** (2021) 992, [arXiv:2106.02056].

67. M. J. Reid *et. al.*, *Trigonometric Parallaxes of High Mass Star Forming Regions: the Structure and Kinematics of the Milky Way*, *Astrophys. J.* **783** (2014) 130, [arXiv:1401.5377].

68. A. J. Deason, A. Fattahi, *et. al.*, *The local high-velocity tail and the galactic escape speed*, *MNRAS* **485** (2019) 3514–3526, [arXiv:1901.02016].

69. GAMBIT Scanner Workgroup: G. D. Martinez, J. McKay, *et. al.*, *Comparison of statistical sampling methods with ScannerBit, the GAMBIT scanning module*, *Eur. Phys. J. C* **77** (2017) 761, [arXiv:1705.07959].

70. GAMBIT Collaboration: P. Athron, C. Balázs, *et. al.*, *Status of the scalar singlet dark matter model*, *Eur. Phys. J. C* **77** (2017) 568, [arXiv:1705.07931].

71. DARWIN: J. Aalbers *et. al.*, *DARWIN: towards the ultimate dark matter detector*, *JCAP* **1611** (2016) 017, [arXiv:1606.07001].

72. P. Scott, *Pippi – painless parsing, post-processing and plotting of posterior and likelihood samples*, *Eur. Phys. J. Plus* **127** (2012) 138, [arXiv:1206.2245].

73. GAMBIT Collaboration: P. Athron, C. Balázs, *et. al.*, *GAMBIT: The Global and Modular Beyond-the-Standard-Model Inference Tool. Addendum for GAMBIT 1.1: Mathematica backends, SUSYHD interface and updated likelihoods*, *Eur. Phys. J. C* **78** (2018) 98, [arXiv:1705.07908]. Addendum to [58].